SIAM J. APPL. MATH.
Vol. 65, No. 2, pp. 494–520

PARAMETRIC RESONANCE IN IMMERSED ELASTIC BOUNDARIES*

RICARDO CORTEZ†, CHARLES S. PESKIN‡,
JOHN M. STOCKIE§, AND DOUGLAS VARELA¶

Abstract. In this paper, we investigate the stability of a fluid-structure interaction problem in which a flexible elastic membrane immersed in a fluid is excited via periodic variations in the elastic stiffness parameter. This model can be viewed as a prototype for active biological tissues such as the basilar membrane in the inner ear, or heart muscle fibers immersed in blood. Problems such as this, in which the system is subjected to internal forcing through a parameter, can give rise to "parametric resonance." We formulate the equations of motion in two dimensions using the immersed boundary formulation. Assuming small amplitude motions, we can apply Floquet theory to the linearized equations and derive an eigenvalue problem whose solution defines the marginal stability boundaries in parameter space. The eigenvalue equation is solved numerically to determine values of fiber stiffness and fluid viscosity for which the problem is linearly unstable. We present direct numerical simulations of the fluid-structure interaction problem (using the immersed boundary method) that verify the existence of the parametric resonances suggested by our analysis.

Key words. immersed boundary, fluid-structure interaction, parametric resonance

AMS subject classifications. 35B34, 35B35, 74F10, 76D05

DOI. 10.1137/S003613990342534X

1. Introduction.

Fluid-structure interaction problems abound in industrial applications as well as in many natural phenomena. Owing to the potentially complex, time-varying geometry and the nonlinear interactions that arise between fluid and solid, such problems represent a major challenge to both mathematical modelers and computational scientists.

This paper deals with a model for fluid-structure interaction known as the immersed boundary (IB) formulation [20], which has proven particularly effective for dealing with complex problems in biological fluid mechanics. In this formulation, the immersed structure is treated as an elastic surface or interwoven mesh of elastic fibers that exert a singular force on a surrounding viscous fluid, while also moving with the velocity of adjacent fluid particles. The associated immersed boundary method has been used to solve a wide range of problems such as blood flow in the heart and arteries [2, 21], swimming microorganisms [8], biofilms [7], and insect flight [16]. More recently, the IB method has also been extended to a much wider range of nonbiological problems involving flow past solid cylinders [12], flapping filaments [29], parachutes [10], and suspensions of flexible particles [25].

*Received by the editors March 31, 2003; accepted for publication (in revised form) February 4, 2004; published electronically December 16, 2004. This work was partially supported by NSF grants DMS-0094179 (Cortez) and DMS-9980069 (Peskin), NSERC grant RGP-238776-01 (Stockie), and the Center for Computational Science at Tulane and Xavier Universities grant DE-FG02-01ER63119 (Cortez).

http://www.siam.org/journals/siap/65-2/42534.html

†Department of Mathematics, Tulane University, 6823 St. Charles Ave., New Orleans, LA 70118 (cortez@math.tulane.edu).

‡Courant Institute of Mathematical Sciences, New York University, 251 Mercer Street, New York, NY 10012 (peskin@cims.nyu.edu).

§Department of Mathematics, Simon Fraser University, 8888 University Drive, Burnaby, BC V5A 1S6, Canada (stockie@math.sfu.ca).

¶Department of Engineering and Applied Science, California Institute of Technology, Pasadena, CA 91125 (vladimir@its.caltech.edu).

While a significant body of literature has developed around numerical simulations using the IB method (as well as related methods such as the blob projection method [4]), comparatively little work has been done on analyzing the stability behavior of solutions to the underlying equations of motion. Beyer and LeVeque [3] were the first to perform an analysis of the IB formulation in one spatial dimension. Stockie and Wetton [26] investigated the linear stability of a flat fiber in two dimensions which is subjected to a small sinusoidal perturbation, and presented asymptotic results on the frequency and rate of decay for the resulting oscillations. Cortez and Varela [5] performed a nonlinear analysis for a perturbed circular elastic membrane immersed in an inviscid fluid.

In all of this previous work, the immersed boundary was assumed to be passive, moving along with the flow and generating forces only in response to elastic deformation. However, there are many problems in which the immersed boundary is an active material, generating time-dependent forces to drive its motion. Examples include beating heart muscle fibers and flagellated cells, both of which apply periodic forces to direct their motion and that of the surrounding fluid.

It is then natural to ask whether periodic forcing at various frequencies will give rise to resonance. In the case of immersed boundaries, the applied force is *internal*, in the sense that the system is forced through a periodic variation in a system parameter (namely, the elastic properties of the solid material) rather than through an external body force. In contrast to externally forced systems, these internally or parametrically forced systems are known to exhibit parametric resonance, in which the response for linear systems (i.e., assuming small amplitude motions) can become unbounded even in the presence of viscous damping. Once nonlinearities are taken into account, however, the response remains bounded, but the system can still exhibit large-amplitude motion when forced at certain resonant frequencies. Analyses of parametric resonance have appeared for various fluid flows involving surface or interfacial waves wherein the system is forced through gravitational modulation [11, 14, 17] or time-dependent heating [15]. However, to our knowledge there has been no analysis performed on fluid-structure problems that captures the two-way interaction between a fluid and an immersed, flexible structure. In a recent study by Wang [28], an analysis is performed of flutter and buckling instabilities in a paper making headbox, in which a long, flexible vane is driven to vibrate under the influence of periodic forcing from turbulent fluid jets. However, the author assumes a given fluid velocity and that the solid structure has no influence on the fluid motion.

In this paper, we perform an analysis of parametric resonance in a two-dimensional, circular, elastic membrane immersed in Navier–Stokes flow, which is driven by a time-periodic variation in its elastic stiffness parameter. The elastic membrane is under tension due to the incompressible fluid it encloses, and the changes in the elastic stiffness parameter are equivalent to changes in the tension of the membrane that mimic the contraction of biological fibers. The novelty of this work is that it includes the full, two-way interaction between the fluid and the membrane. In sections 2 and 3, we present the linearized equations of motion for the IB formulation and reduce them to a suitable nondimensional form. In sections 4, 5, and 6, we perform a Floquet analysis of the problem and derive a system of equations that relate the amplitude, frequency, and wavenumber of the internal forcing to the physical parameters in the problem. The natural modes for the unforced system are derived in section 7 and compared to the asymptotic expressions for the natural modes in a flat fiber that were derived in [26]. We also compare the natural modes to those observed in computations using the blob projection method, an alternate method for solving the IB problem that

affords higher spatial accuracy. In section 8 we consider the periodically forced problem and determine the conditions under which parametric resonance can occur. The results are verified using numerical simulations with the IB method.

2. Problem definition. Consider an elastic fiber immersed in a two-dimensional, viscous, incompressible fluid of infinite extent. The fiber is a closed loop with resting length of zero, so that in the absence of fluid the fiber would shrink to a point. However, because an incompressible fluid occupies the region inside the fiber, the equilibrium state is a circle of constant radius R, in which the pressure drop across the fiber is balanced by the tension force. Our aim is to investigate a *parametric excitation* of the fiber, in which the elastic stiffness is varied periodically in time.

The equations of motion for the fluid and immersed boundary can be written in terms of the vorticity $\xi(\boldsymbol{x},t)$ and stream function $\psi(\boldsymbol{x},t)$ as [19, p. 1]:

$$\rho\left(\xi_t + \boldsymbol{u}\cdot\nabla\xi\right) = \mu\nabla^2\xi + \hat{\boldsymbol{z}}\cdot\nabla\times\boldsymbol{f}, \tag{2.1a}$$

$$\boldsymbol{u} = -\hat{\boldsymbol{z}}\times\nabla\psi, \tag{2.1b}$$

$$-\nabla^2\psi = \xi, \tag{2.1c}$$

$$\boldsymbol{f}(\boldsymbol{x},t) = \int_0^{2\pi} (K\boldsymbol{X}_s)_s\,\delta(\boldsymbol{x}-\boldsymbol{X})\,ds, \tag{2.1d}$$

$$\boldsymbol{X}_t = \boldsymbol{u}(\boldsymbol{X},t), \tag{2.1e}$$

where $\boldsymbol{x} = (x,y)$ and $\hat{\boldsymbol{z}} = (0,0,1)$. The fluid velocity $\boldsymbol{u}(\boldsymbol{x},t)$ and fiber force $\boldsymbol{f}(\boldsymbol{x},t)$ are functions of position and time, whereas the fiber position $\boldsymbol{X}(s,t) = (X^r(s,t), X^\theta(s,t))$ is a function of time and the Lagrangian fiber parameter $0 \le s \le 2\pi$ (which is the same as the angle θ when the fiber's reference state is a circle). We assume in this paper that the stiffness is a periodic function of time,

$$K = K(s,t) = K_c(1 + 2\tau\sin\omega_o t), \tag{2.2}$$

which has no dependence on the spatial variable s.

We point out that s is a Lagrangian parameter and is not necessarily proportional to arclength since the fiber is allowed to stretch and shrink tangentially. The force density $(K\boldsymbol{X}_s)_s$ thus includes components normal and tangential to the fiber. If we identify the tension $T(s) = K\|\boldsymbol{X}_s\|$ and the unit tangent vector $\hat{\tau}(s) = \boldsymbol{X}_s/\|\boldsymbol{X}_s\|$, we may write the force density term as

$$(K\boldsymbol{X}_s)_s = (T(s)\hat{\tau}(s))_s = T_s(s)\hat{\tau}(s) + T(s)\hat{\tau}_s(s),$$

which shows explicitly that the force resolves itself into normal and tangential components. We also remark that spatial dependence in K can be easily incorporated into our analysis provided that the spatial variations are small (that is, on the order of the parameter ϵ introduced in the following section).

Our motivation comes from active muscle fibers that may contract and relax to generate fluid motion. For this reason we will focus on nonnegative values of the stiffness and we will be concerned mostly with the range $0 \le \tau \le \frac{1}{2}$ in (2.2). However, our analysis does not require this restriction and the results apply to values of $\tau > 1/2$ as well. This is important because there are instances in which a negative stiffness plays an important role as is the case of hair bundles in the bullfrog inner ear [9].

3. Nondimensionalization. We first simplify the problem by scaling the variables and forming dimensionless groups. For now, variables with a tilde will be dimensionless. Let

$$\begin{aligned} \boldsymbol{x} &= R\,\tilde{\boldsymbol{x}}, \\ \boldsymbol{u} &= U\,\tilde{\boldsymbol{u}} \qquad (U \text{ will be determined later}), \\ t &= R/U\,\tilde{t}, \\ K &= K_c\,\tilde{K}, \end{aligned}$$

which imply that

$$\begin{aligned} \boldsymbol{f}(\boldsymbol{x},t) = \frac{K_c}{R}\,\tilde{\boldsymbol{f}}(\tilde{\boldsymbol{x}},\tilde{t}) &= \int_0^{2\pi} (\tilde{K}\tilde{\boldsymbol{X}}_s)_s\,\delta(\tilde{\boldsymbol{x}}-\tilde{\boldsymbol{X}})\,ds, \\ \xi = \frac{U}{R}\,\tilde{\xi}, \\ \psi = UR\,\tilde{\psi}. \end{aligned}$$

With these scalings the vorticity equation becomes

$$\tilde{\xi}_{\tilde{t}} + \tilde{\boldsymbol{u}}\cdot\tilde{\nabla}\,\tilde{\xi} = \left(\frac{\mu}{\rho U R}\right)\tilde{\nabla}^2\tilde{\xi} + \left(\frac{K_c}{\rho U^2}\right)\,(\hat{\boldsymbol{z}}\cdot\tilde{\nabla}\times\tilde{\boldsymbol{f}}).$$

In view of this and (2.2), we now define

$$U = R\omega_o, \qquad \nu = \frac{\mu}{\rho U R} = \frac{\mu}{\rho R^2\omega_o}, \qquad \kappa = \frac{K_c}{\rho U^2} = \frac{K_c}{\rho R^2\omega_o^2}, \tag{3.1}$$

so that the unperturbed fiber configuration is the unit circle ($\boldsymbol{X} = \hat{\boldsymbol{r}}(s)$) and we can write the dimensionless equations (omitting the tildes) as

$$\xi_t + \boldsymbol{u}\cdot\nabla\,\xi = \nu\nabla^2\xi + \kappa(\hat{\boldsymbol{z}}\cdot\nabla\times\boldsymbol{f}), \tag{3.2a}$$

$$\boldsymbol{u} = -\hat{\boldsymbol{z}}\times\nabla\psi, \tag{3.2b}$$

$$-\nabla^2\psi = \xi, \tag{3.2c}$$

$$\boldsymbol{f}(\boldsymbol{x},t) = \int_0^{2\pi} (K\boldsymbol{X}_s)_s\,\delta(\boldsymbol{x}-\boldsymbol{X})\,ds, \tag{3.2d}$$

$$\boldsymbol{X}_t = \boldsymbol{u}(\boldsymbol{X},t), \tag{3.2e}$$

with

$$K = (1 + 2\tau\sin t), \tag{3.3a}$$

$$\boldsymbol{X} = \hat{\boldsymbol{r}}(s) + \epsilon\boldsymbol{X}_1^{(1)}(s,t) + \cdots. \tag{3.3b}$$

Our aim is now to solve (3.2a)–(3.2e) with the only two remaining parameters, ν and κ, defined in (3.1). We point out that ν is the reciprocal of the Reynolds number and κ is the square of the natural frequency divided by the driving frequency.

4. Small-amplitude approximation. For the linear analysis, assume the fiber force can be written as

$$\boldsymbol{f} = \boldsymbol{f}^{(0)}(\boldsymbol{x},t) + \epsilon\boldsymbol{f}^{(1)}(\boldsymbol{x},t) + \cdots,$$

so that the term $(\hat{\boldsymbol{z}} \cdot \nabla \times \boldsymbol{f})$ in (3.2a) can be expanded as

$$(\hat{\boldsymbol{z}} \cdot \nabla \times \boldsymbol{f}) = (\hat{\boldsymbol{z}} \cdot \nabla \times \boldsymbol{f}^{(0)}) + \epsilon(\hat{\boldsymbol{z}} \cdot \nabla \times \boldsymbol{f}^{(1)}) + \cdots.$$

CLAIM 1. *Given the expansions in* (3.3a) *and* (3.3b),

$$(\hat{\boldsymbol{z}} \cdot \nabla \times \boldsymbol{f}^{(0)}) = 0 \qquad \textit{and}$$
$$(\hat{\boldsymbol{z}} \cdot \nabla \times \boldsymbol{f}^{(1)}) = K(t)\left(X^{\theta}_{ss} + X^{r}_{s}\right)\left(\frac{\delta(r-1)}{r}\right)_r - K(t)\left(X^{r}_{sss} - X^{\theta}_{ss}\right)\frac{\delta(r-1)}{r}.$$

The proof is found in Appendix B.

Since the leading-order term in the curl of the force is zero, the corresponding flow is simply the trivial solution $\xi^{(0)} = \psi^{(0)} = 0$. Therefore, we look for a series solution expanded in terms of powers of a small parameter ϵ:

$$\xi = \epsilon\, \xi^{(1)}(\boldsymbol{x}, t) + \cdots,$$
$$\psi = \epsilon\, \psi^{(1)}(\boldsymbol{x}, t) + \cdots.$$

In the remainder of this work, we assume ϵ is small and consider the $O(\epsilon)$ equations

$$\text{(4.1a)}\quad \xi_t = \nu\nabla^2\xi + \kappa K(t)\left(X^{\theta}_{ss} + X^{r}_{s}\right)\left[\frac{\delta(r-1)}{r}\right]_r - \kappa K(t)\left(X^{r}_{sss} - X^{\theta}_{ss}\right)\frac{\delta(r-1)}{r},$$
$$\text{(4.1b)}\quad \nabla^2\psi = -\xi,$$
$$\text{(4.1c)}\quad X^{r}_{t} = \psi_{\theta}\big|_{r=1},$$
$$\text{(4.1d)}\quad X^{\theta}_{t} = -\psi_{r}\big|_{r=1},$$

where we have omitted the superscript $^{(1)}$ on most variables because we will be working solely with these quantities from now on.

It is worthwhile mentioning that in the above expansions, the influence of the time-dependent stiffness coefficient is felt solely at first order in ϵ, and so we need only consider the forcing terms up to $O(\epsilon)$. The derivation can be easily extended to include the case where the stiffness is spatially dependent, for which the s-variation appears as an order ϵ perturbation of a time-dependent stiffness,

$$K = K(s,t) = K^{(0)}(t) + \epsilon K^{(1)}(s,t) + O(\epsilon^2).$$

When a Floquet-type expansion is assumed for $K^{(1)}(s,t)$ (refer to the next section), correction terms appear in the $O(\epsilon)$ equations, and these corrections complicate the analysis somewhat by coupling together the various spatial modes. We do not consider a spatially dependent stiffness in this paper.

It is quite striking that a spatially homogeneous $K(t)$ can have any interesting effects in this problem. This is because such $K(t)$ would have no effect at all on the equilibrium state in which the fiber is a circle. Starting with that equilibrium state as initial data and imposing time-periodic $K(t)$ will produce only an oscillation of the pressure and no motion of the fiber at all. But if instead we start with an initial condition that is arbitrarily close but not exactly equal to a circular equilibrium state, we can nevertheless build up a large-amplitude and spatially inhomogeneous oscillation of the fiber through the application of spatially homogeneous but time-periodic $K(t)$ at the right driving frequency. This is actually typical of parametric

resonance. A pendulum that is initially at rest hanging straight down cannot be made to swing by imposing periodic changes in its length, but a pendulum that is initially swinging ever so slightly can indeed be made to swing violently by the application of precisely such changes in length, as every child who swings in the playground knows [6].

5. Floquet analysis. Since we are not simply looking for natural modes but rather are investigating the response of the system to a periodic forcing with a given frequency, we must look for a solution in the form of an infinite series. This is a very general approach in Floquet theory [18], and our derivation parallels the analysis of Kumar and Tuckerman [11] for a horizontal fluid interface consisting of two fluids with different densities. It is worth mentioning that other approaches have also been used to study parametric resonances. For example, Semler and Païdoussis [23] analyze the case of a tubular beam filled with fluid whose velocity contains sinusoidal fluctuations. They use separation of variables and nonlinear dynamics techniques to solve the perturbation equations for small amplitude fluctuations. We will see that our approach will result in a system of equations in block form that is very similar to the equations derived in [23].

We assume that the unknown functions can be written as series of the following form:

$$\begin{aligned}
\xi(r,\theta,t) &= e^{ip\theta}\sum_{n=-\infty}^{\infty}\xi_n(r)e^{(\gamma+in)t},\\
\psi(r,\theta,t) &= e^{ip\theta}\sum_{n=-\infty}^{\infty}\psi_n(r)e^{(\gamma+in)t},\\
X^r(\theta,t) &= e^{ip\theta}\sum_{n=-\infty}^{\infty}X^r_n e^{(\gamma+in)t},\\
X^\theta(\theta,t) &= e^{ip\theta}\sum_{n=-\infty}^{\infty}X^\theta_n e^{(\gamma+in)t},
\end{aligned}$$

where $i=\sqrt{-1}$, p is an integer with $p>1$, and $\gamma=\alpha+i\beta$ with α and β real. To simplify the notation, we define $\mathcal{E}_n \doteq e^{(\gamma+in)t+ip\theta}$ and then write the equation for the vorticity from (4.1a) as

$$\begin{aligned}
\sum_{n=-\infty}^{\infty}\left((\gamma+in)+\frac{\nu p^2}{r^2}\right)\xi_n\mathcal{E}_n \;=\; \sum_{n=-\infty}^{\infty}\Bigg\{&\frac{\nu}{r}(r\xi_n')' + \kappa K(-p^2X_n^\theta + ipX_n^r)\left(\frac{\delta(r-1)}{r}\right)'\\
&+\kappa K(ip^3X_n^r - p^2X_n^\theta)\,\frac{\delta(r-1)}{r}\Bigg\}\mathcal{E}_n. \qquad (5.1)
\end{aligned}$$

Except for the stiffness $K(t)$, all of the t- and θ-dependence is now encompassed by the factor $\mathcal{E}_n$. Note that ξ_n and ψ_n are functions of r, while X_n^r and X_n^θ are constants. The primes in the equations denote derivatives with respect to r. If we take advantage of the fact that the stiffness from (3.3a) can be rewritten as

$$K(t) = 1 - i\tau e^{it} + i\tau e^{-it} \qquad (5.2)$$

and then rearrange terms in the series in (5.1) and divide by $\mathcal{E}_n$, we obtain

$$-\frac{1}{r}(r\xi_n')' + \left(\frac{(\gamma+in)}{\nu} + \frac{p^2}{r^2}\right)\xi_n \tag{5.3}$$
$$= \frac{\kappa}{\nu}\left(\frac{\delta(r-1)}{r}\right)'\left[-p^2\left(X_n^\theta - i\tau X_{n-1}^\theta + i\tau X_{n+1}^\theta\right) + ip\left(X_n^r - i\tau X_{n-1}^r + i\tau X_{n+1}^r\right)\right]$$
$$+ \frac{\kappa}{\nu}\frac{\delta(r-1)}{r}\left[-p^2\left(X_n^\theta - i\tau X_{n-1}^\theta + i\tau X_{n+1}^\theta\right) + ip^3\left(X_n^r - i\tau X_{n-1}^r + i\tau X_{n+1}^r\right)\right]$$

for all integer values of n. The equations for the remaining unknowns in (4.1b)–(4.1d) do not involve $K(t)$, and so for the nth coefficient functions we have

$$-\frac{1}{r}(r\psi_n')' + \frac{p^2}{r^2}\psi_n = \xi_n,$$
$$(\gamma+in)X_n^r = ip\psi_n(1),$$
$$(\gamma+in)X_n^\theta = -\psi_n'(1).$$

A more useful formulation of the problem is in terms of jump conditions across the fiber. The delta function terms in (5.3) are nonzero only on the fiber, and so the following two equations hold on either side of the fiber:

$$-\frac{1}{r}(r\xi_n')' + \left(\frac{(\gamma+in)}{\nu} + \frac{p^2}{r^2}\right)\xi_n = 0, \tag{5.4a}$$
$$-\frac{1}{r}(r\psi_n')' + \frac{p^2}{r^2}\psi_n = \xi_n. \tag{5.4b}$$

The fiber evolution equations hold on the fiber (at $r = 1$):

$$(\gamma+in)X_n^r = ip\psi_n(1), \tag{5.4c}$$
$$(\gamma+in)X_n^\theta = -\psi_n'(1). \tag{5.4d}$$

At the same time, the jump conditions connect the solutions on either side of the fiber (see Appendix C):

$$[\![\xi_n]\!] = \frac{\kappa}{\nu}\left[p^2\left(X_n^\theta - i\tau X_{n-1}^\theta + i\tau X_{n+1}^\theta\right) - ip\left(X_n^r - i\tau X_{n-1}^r + i\tau X_{n+1}^r\right)\right], \tag{5.4e}$$
$$[\![\xi_n']\!] = -\frac{i\kappa p(p^2-1)}{\nu}\left(X_n^r - i\tau X_{n-1}^r + i\tau X_{n+1}^r\right), \tag{5.4f}$$
$$[\![\psi_n]\!] = 0, \tag{5.4g}$$
$$[\![\psi_n']\!] = 0, \tag{5.4h}$$

where we denote the jump in a quantity q by $[\![q]\!] = q|_{r=1^+} - q|_{r=1^-}$. These jump conditions were found in the same way as in [13, 22], by integrating the equations for vorticity across the fiber. We point out that this system of equations cannot be reduced to a Mathieu equation (see [11]).

6. Solution of the vorticity and stream function equations. The equations (5.4) from the previous section can be solved explicitly for each integer value of n, both inside and outside the fiber. Due to (5.4c) and (5.4d), the character of the solution will be different depending on whether the quantity $(\gamma + in)$ is zero. This will happen for $n = 0$ whenever $\gamma = 0$. We therefore solve the equations considering two cases.

6.1. Case $(\gamma+in) \neq 0$. If we make the change of variables $z^2 = -r^2(\gamma+in)/\nu$, then (5.4a) turns into the Bessel equation

$$z^2\xi_n''(z) + z\xi_n'(z) + [z^2 - p^2]\xi_n(z) = 0.$$

The appropriate solution, rewritten in terms of r, is [27]

$$\xi_n(r) = \begin{cases} b_n J_p(i\Omega_n r) & \text{if } r < 1 \qquad \text{(inner)}, \\ a_n H_p(i\Omega_n r) & \text{if } r > 1 \qquad \text{(outer)}, \end{cases}$$

where $\Omega_n \doteq \sqrt{(\gamma+in)/\nu}$ is chosen as the square root with positive real part, $J_p(z)$ is the Bessel function of the first kind, $H_p(z) = J_p(z) + iY_p(z)$ is the Hankel function of the first kind, and a_n and b_n are arbitrary constants (see Appendix A).

The corresponding stream function is given by (see Appendix D)

$$\psi_n(r) = \frac{1}{2ip\Omega_n} \begin{cases} b_n r\Big[J_{p-1}(i\Omega_n r) + J_{p+1}(i\Omega_n r)\Big] \\ \qquad + r^p\Big[a_n H_{p-1}(i\Omega_n) - b_n J_{p-1}(i\Omega_n)\Big] \text{ if } 0 \le r < 1, \\ a_n r\Big[H_{p-1}(i\Omega_n r) + H_{p+1}(i\Omega_n r)\Big] \\ \qquad - r^{-p}\Big[a_n H_{p+1}(i\Omega_n) - b_n J_{p+1}(i\Omega_n)\Big] \text{ if } r > 1. \end{cases}$$

One can easily check that $\psi_n(r)$ and $\psi_n'(r)$ are continuous across the boundary and that

$$\psi_n(1) = \frac{1}{2ip\Omega_n}\Big[a_n H_{p-1}(i\Omega_n) + b_n J_{p+1}(i\Omega_n)\Big],$$
$$\psi_n'(1) = \frac{1}{2i\Omega_n}\Big[a_n H_{p-1}(i\Omega_n) - b_n J_{p+1}(i\Omega_n)\Big].$$

Turning now to (5.4c) and (5.4d), we find the fiber position to be

$$X_n^r = \frac{1}{2\nu\Omega_n^3}\Big[a_n H_{p-1}(i\Omega_n) + b_n J_{p+1}(i\Omega_n)\Big],$$
$$X_n^\theta = \frac{-1}{2i\nu\Omega_n^3}\Big[a_n H_{p-1}(i\Omega_n) - b_n J_{p+1}(i\Omega_n)\Big].$$

We can solve for a_n and b_n from these equations to find

$$a_n = \frac{\nu\Omega_n^3}{H_{p-1}(i\Omega_n)}\left(X_n^r - iX_n^\theta\right),$$
$$b_n = \frac{\nu\Omega_n^3}{J_{p+1}(i\Omega_n)}\left(X_n^r + iX_n^\theta\right).$$

We now substitute these expressions into the jump conditions (5.4e)–(5.4f) to get the following system of equations:

$$\begin{aligned} 0 = {} & i\left\{\phi\ \Omega_n^3\left[\frac{H_p(i\Omega_n)}{H_{p-1}(i\Omega_n)} - \frac{J_p(i\Omega_n)}{J_{p+1}(i\Omega_n)}\right] + ip\right\} X_n^r \\ & + \left\{\phi\ \Omega_n^3\left[\frac{H_p(i\Omega_n)}{H_{p-1}(i\Omega_n)} + \frac{J_p(i\Omega_n)}{J_{p+1}(i\Omega_n)}\right] - ip^2\right\} X_n^\theta \\ & + i\tau p\left(X_{n-1}^r - X_{n+1}^r\right) - \tau p^2\left(X_{n-1}^\theta - X_{n+1}^\theta\right), \end{aligned} \tag{6.1}$$

$$
\begin{aligned}
0 = i\left\{\phi\ \Omega_n^4\left[2 - \frac{H_{p+1}(i\Omega_n)}{H_{p-1}(i\Omega_n)} - \frac{J_{p-1}(i\Omega_n)}{J_{p+1}(i\Omega_n)}\right] + 2p(p^2-1)\right\} X_n^r \\
- \phi\ \Omega_n^4\left[\frac{H_{p+1}(i\Omega_n)}{H_{p-1}(i\Omega_n)} - \frac{J_{p-1}(i\Omega_n)}{J_{p+1}(i\Omega_n)}\right] X_n^\theta \\
+ 2\tau p(p^2-1)\left(X_{n-1}^r - X_{n+1}^r\right),
\end{aligned} \tag{6.2}
$$

where we define ϕ as the grouping $\phi = \nu^2/\kappa$. It is these last two equations, (6.1) and (6.2), that determine the coefficients X_n^r and X_n^θ in the case when $(\gamma + in) \neq 0$.

6.2. Case $(\gamma + in) = 0$. For this case, the vorticity equation becomes

$$r^2\xi_n''(r) + r\xi_n'(r) - p^2\xi_n(r) = 0,$$

whose appropriate solution is

$$\xi_o(r) = \begin{cases} b_o r^p & \text{if } r < 1 \qquad \text{(inner)}, \\ a_o r^{-p} & \text{if } r > 1 \qquad \text{(outer)}, \end{cases}$$

while the corresponding solution for the stream function is

$$\psi_o(r) = \begin{cases} \dfrac{1}{4p}\left(b_o - \dfrac{a_o}{1-p}\right) r^p - \dfrac{b_o}{4(1+p)} r^{2+p} & \text{if } r < 1, \\ \dfrac{1}{4p}\left(\dfrac{b_o}{1+p} - a_o\right) r^{-p} - \dfrac{a_o}{4(1-p)} r^{2-p} & \text{if } r > 1. \end{cases}$$

One can easily check that $\psi_o(r)$ and $\psi_o'(r)$ are continuous across the boundary and that

$$\psi_o(1) = \frac{1}{4p}\left[\frac{a_o}{p-1} + \frac{b_o}{p+1}\right],$$
$$\psi_o'(1) = \frac{1}{4}\left[\frac{a_o}{p-1} - \frac{b_o}{p+1}\right].$$

Turning now to (5.4c) and (5.4d), we find that in this case, the above equations reduce to $\psi_o(1) = \psi_o'(1) = 0$, which implies that $a_o = b_o = 0$. This means that when $(\gamma + in) = 0$ we obtain the trivial solution $\xi_o(r) \equiv 0$ and $\psi_o(r) \equiv 0$. The jump conditions (5.4e) and (5.4f) then give the system of equations

$$0 = ip^2\left(X_n^\theta - i\tau X_{n-1}^\theta + i\tau X_{n+1}^\theta\right) + p\left(X_n^r - i\tau X_{n-1}^r + i\tau X_{n+1}^r\right), \tag{6.3}$$

$$0 = ip(p^2-1)\left(X_n^r - i\tau X_{n-1}^r + i\tau X_{n+1}^r\right), \tag{6.4}$$

which are used instead of (6.1)–(6.2) for the case $(\gamma + in) = 0$.

7. Natural modes for the unforced fiber. When there is no forcing applied to the fiber, then $\tau = 0$ and there is no need to look for a solution in the form of an infinite series. Instead, we can consider a single mode by taking $n = 0$, for which the problem reduces to the following single pair of equations for X^r and X^θ:

$$
\begin{aligned}
0 = i\left\{\phi\ \Omega_o^3\left[\frac{H_p(i\Omega_o)}{H_{p-1}(i\Omega_o)} - \frac{J_p(i\Omega_o)}{J_{p+1}(i\Omega_o)}\right] + ip\right\} X^r \\
+ \left\{\phi\ \Omega_o^3\left[\frac{H_p(i\Omega_o)}{H_{p-1}(i\Omega_o)} + \frac{J_p(i\Omega_o)}{J_{p+1}(i\Omega_o)}\right] - ip^2\right\} X^\theta,
\end{aligned} \tag{7.1}
$$

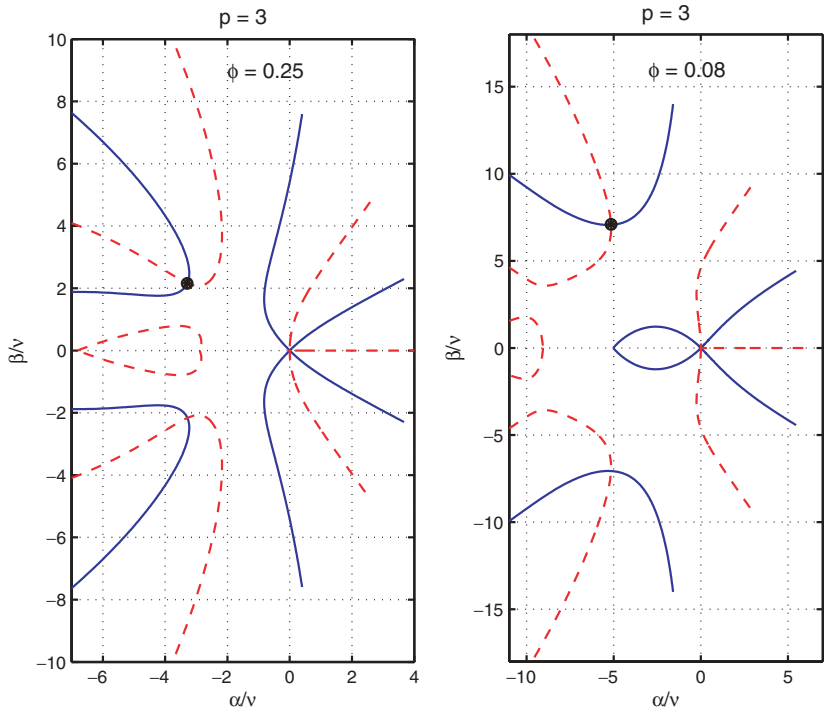

FIG. 7.1. *Zero-level contours of $\mathcal{D}(\Omega_o;\phi,p)$ for $p=3$ and two values of ϕ. The solid lines correspond to the real part and the dashed lines to the imaginary parts. Intersection points represent the natural modes of oscillation of the fiber.*

$$0 = i\left\{\phi\,\Omega_o^4\left[2-\frac{H_{p+1}(i\Omega_o)}{H_{p-1}(i\Omega_o)}-\frac{J_{p-1}(i\Omega_o)}{J_{p+1}(i\Omega_o)}\right]+2p(p^2-1)\right\}X^r \\ -\phi\,\Omega_o^4\left[\frac{H_{p+1}(i\Omega_o)}{H_{p-1}(i\Omega_o)}-\frac{J_{p-1}(i\Omega_o)}{J_{p+1}(i\Omega_o)}\right]X^\theta, \tag{7.2}$$

where $\Omega_o^2=\gamma/\nu=(\alpha/\nu)+i(\beta/\nu)$ and $\phi=\nu^2/\kappa$. Consequently, the above equations can be rewritten as a 2×2, homogeneous, linear system

$$\mathcal{M}\begin{pmatrix}X^r\\X^\theta\end{pmatrix}=0,$$

which has a nontrivial solution only if $\det(\mathcal{M})=0$. For notational convenience we define the function $\mathcal{D}(\Omega_o;\phi,p)=\det(\mathcal{M})$. The roots of $\mathcal{D}(\Omega_o;\phi,p)=0$, which is a *dispersion relation*, correspond to the natural modes of oscillation of the immersed boundary for a given set of parameters ϕ and p.

From the left plot of Figure 7.1, which corresponds to $p=3$ and $\phi=0.25$, a possible value of the natural response is $(\gamma/\nu)=(\alpha/\nu,\beta/\nu)\approx(-3.29,2.16)$. The right plot of Figure 7.1 shows that for $\phi=0.08$ the root is $(\alpha/\nu,\beta/\nu)\approx(-5.15,7.1)$ instead. These roots are in dimensionless form, and the dimensional frequency γ is obtained by multiplying these roots by $\mu/\rho R^2$. Note that in both cases, the natural mode of oscillation is stable (i.e., α is negative), as would be expected from an unforced immersed fiber (see [26]).

7.1. Collapse of the curves. The condition $\mathcal{D}(\Omega_o; \phi, p) = 0$ defines implicitly the root

$$\frac{\gamma}{\nu} = F(\phi, p) \tag{7.3}$$

as a function of the parameters. This suggests that the same root can be obtained with different values of damping ν and stiffness κ, provided the ratio $\phi = \nu^2/\kappa$ is held constant.

We corroborated this with the numerical solution of the nonlinear equations (3.2a)–(3.2e) for different combinations of (ν, κ) that yield the same value of ϕ. The blob projection method described in [4] was used in these calculations, which solves the IB problem using high-order regularized delta functions and fourth-order finite differences and time stepping. We have chosen to use this approach (rather than the IB method described in section 9) since the blob projection method affords higher accuracy, particularly when ϕ is small.

The initial condition of the fiber was the unit circle augmented by a single p-mode perturbation with amplitude ϵ, so that the fiber configuration can be written in polar coordinates as

$$r(\theta, t) = 1 + \epsilon B(t) \cos(p\theta) + O(\epsilon^2).$$

After each run, the amplitude $B(t)$ was assumed to have the form $B(t) = e^{\alpha t}[\cos(\beta t) + (\alpha/\beta)\sin(\beta t)]$ because this function has zero slope at $t = 0$ and it oscillates with decaying amplitude. The values of (α, β) can then be estimated numerically using least squares. These values were then compared with the roots of (7.3). This procedure was repeated for several values of ϕ with perturbed modes $p = 2$, 3, and 4, and the results are summarized in Figure 7.2.

The analytical results (plotted as solid lines) correspond very well with the numerical calculations (plotted as points). Two simulations corresponding to different combinations of ν and κ are performed for every ϕ. The observed values of α and β corresponding to a given ϕ are nearly identical, so that the points cannot be distinguished visually in Figure 7.2. Consequently, ϕ is an appropriate parameter for characterizing the fiber oscillations.

The correspondence between the analytical and computed results is very good for most values of the parameters, except for relatively large values of ϕ. This is mostly due to the fact that the blob projection method is implemented with periodic boundary conditions in a box about twice as large as the fiber's diameter. For large values of ϕ, the diffusion is significant over the time scale of the runs, and the dynamics are affected by the periodicity. Nonetheless, the results clearly show that different values of (ν, κ) that yield the same ϕ give the same root.

7.2. The small viscosity limit. We consider the limit of small viscosity by assuming a fixed value of the stiffness κ and small value of ν. It will be convenient to define a natural response frequency by $\omega_N \doteq \sqrt{p(p^2-1)/2}$, which is displayed in the frequency plot in Figure 7.2 as a dashed line for comparison with the analytical and computed results discussed in the preceding section. In the small viscosity case, (7.3), whose roots represent the dispersion relation, can be expanded as a series in powers of ν. The results show that the first few terms in the expansion of the natural response of the fiber are

$$\alpha = -\frac{p}{2\sqrt{2}}\omega_N^{1/2}\kappa^{1/4}\sqrt{\nu} + \frac{(p^3 - 3p^2 - p + 1)}{4}\nu + \cdots, \tag{7.4}$$

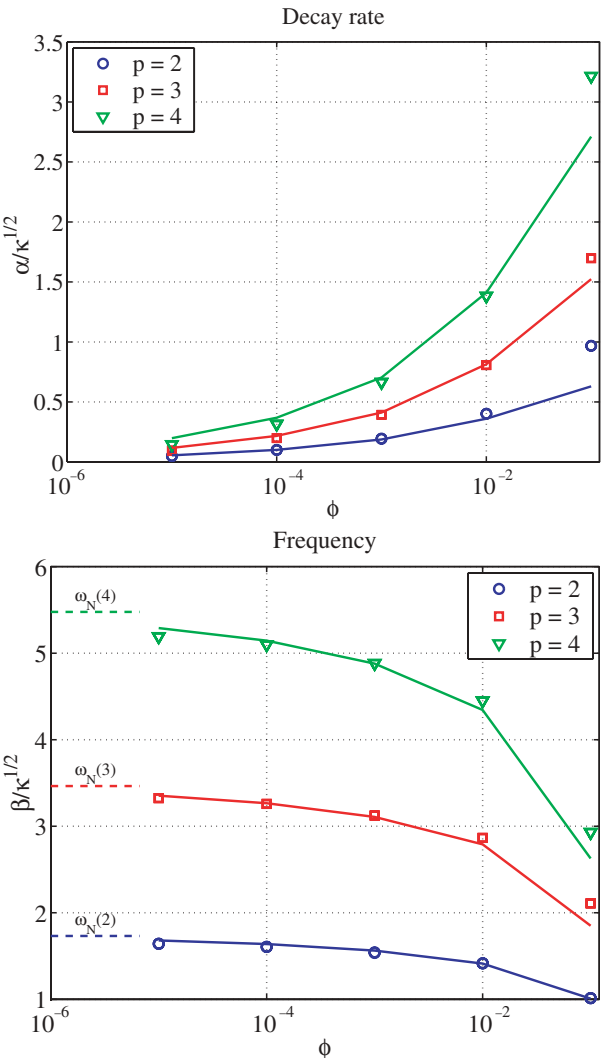

FIG. 7.2. *Roots $\gamma = \alpha + i\beta$ of the dispersion relation $\mathcal{D}(\Omega_o; \phi, p) = 0$, plotted as scaled values of α and β versus ϕ. The analytical results are displayed as solid lines, while the numerical approximations are plotted as points, with multiple points corresponding to simulations done using different values of κ and ν corresponding to the same ϕ. The results are presented for initial fiber perturbations corresponding to three different modes: $p = 2$, 3, and 4. The zero-viscosity ($\phi = 0$) limit, $\omega_N(p) = \sqrt{p(p^2-1)/2}$, is also shown for comparison.*

$$\beta = \omega_N\sqrt{\kappa} - \frac{p}{2\sqrt{2}}\omega_N^{3/4}\kappa^{1/4}\sqrt{\nu} - \frac{p(4p^3 - 39p^2 - 4p + 8)}{64\sqrt{2}}\omega_N^{1/4}\kappa^{-1/4}\nu^{3/2} + \cdots. \tag{7.5}$$

In the limit as $\nu \to 0$, these become $\alpha = 0$ and $\beta = \omega_N\sqrt{\kappa}$, which is precisely the linear dispersion relation found by other methods in [5] for a closed membrane in Euler flow.

It is also possible to compare the above expressions to the asymptotic expansions derived in [26] for an unforced, horizontal fiber immersed in a viscous fluid. The normal mode of oscillation for the flat fiber initialized with a p-mode obeys the following

to leading order:

$$\alpha \sim -2^{-7/4}\,\rho^{-3/4}\,\mu^{1/2}\,K_c^{1/4}\,p^{7/4}\,R^{-3/2} = -p\left(\frac{p^3}{2^7}\right)^{1/4}\left(\frac{\mu}{\rho R^2}\right)^{1/2}\left(\frac{K_c}{\rho R^2}\right)^{1/4},$$

$$\beta \sim 2^{-1/2}\,\rho^{-1/2}\,K_c^{1/2}\,p^{3/2}\,R^{-1} = \left(\frac{p^3}{2}\right)^{1/2}\left(\frac{K_c}{\rho R^2}\right)^{1/2}.$$

Substituting the nondimensional variables from (3.1) into (7.4) and (7.5), it is possible to show that the parameter dependence in the first term in each of α and β is identical to that in the expressions above, provided that we take $\omega_o \equiv 1$. We note that the natural frequency of the flat fiber is different from ω_N above due to the differences in the geometry of the problems. Furthermore, the linear theory for the circular fiber excludes the $p = 1$ mode, since to leading order this perturbation results only in a translation of the fiber.

8. Stability of the periodically forced fiber. In Floquet stability theory, the standard approach is to determine solutions with $\mathrm{Re}(\gamma) = \alpha = 0$, which correspond to the boundary of the stability region. In general, we expect the coefficients in (6.1) and (6.2) to decrease in magnitude as n increases, and so it is reasonable to truncate the series expansions at some finite number of terms, say, $-N \le n \le N$ (this is an assumption that will be checked later on). Equations (6.1) and (6.2) are written for $n = \pm 1, \pm 2, \ldots, \pm N$, and (6.3) and (6.4) are written for $n = 0$, which results in a linear system of dimension $(4N + 4) \times (4N + 4)$ for the unknown coefficients X_n^r and X_n^θ.

8.1. The reality condition. In general, the coefficients arising from the solution to the linear system are complex-valued, but the position of the fiber must be a real quantity. We therefore need to impose additional constraints to guarantee that the Floquet expansion

$$X^r(t) = \sum_n X_n^r e^{int}$$

is real. This will also allow the series to be written for positive index only. Consequently,

$$\overline{X}^r(t) = \sum_n \overline{X}_n^r e^{-int} = \sum_n \overline{X}_{-n}^r e^{int} = \sum_n X_n^r e^{int} = X^r(t),$$

which implies that

$$X_{-n}^r = \overline{X}_n^r \quad \text{for every } n.$$

This is the called the *reality condition* (see [11]), and it allows us to consider (6.1) and (6.2) for strictly positive values of n, thereby eliminating the coefficients for $n < 0$. The condition also implies that $X_o^r = \overline{X}_o^r$, for use in (6.3) and (6.4) with $n = 0$. The same reality condition applies to X_n^θ.

8.2. Formulation as an eigenvalue problem. Equations (6.1)–(6.2) now take the form

$$0 = A_n X_n^r + B_n X_n^\theta + \tau\left[C_n X_{n-1}^r + D_n X_{n-1}^\theta + E_n X_{n+1}^r + F_n X_{n+1}^\theta\right].$$

By setting the real part and the imaginary part of the equation to zero independently, we can write the final system as

$$(\mathcal{D} + \tau\, \mathcal{C})\boldsymbol{v} = 0,$$

where $\mathcal{D}$ and $\mathcal{C}$ are *real-valued* matrices, each of dimension $(4N+4)\times(4N+4)$. The vector is $\boldsymbol{v} = [v_0, v_1, v_2, \ldots, v_N]^T$, where each component has four elements, $v_n = [\mathrm{Re}(X_n^r), \mathrm{Im}(X_n^r), \mathrm{Re}(X_n^\theta), \mathrm{Im}(X_n^\theta)]$, with the difference now being that the reality condition ensures that all solution components are real values. The matrices $\mathcal{D}$ and $\mathcal{C}$ have the following block form:

$$\mathcal{D} = \begin{pmatrix} D_0 & 0 & & \ldots & 0 \\ 0 & D_1 & 0 & \ldots & 0 \\ 0 & \ddots & \ddots & \ddots & \vdots \\ \vdots & & 0 & D_{N-1} & 0 \\ 0 & \ldots & & 0 & D_N \end{pmatrix},$$

$$\mathcal{C} = \begin{pmatrix} 0 & C_{01} & & \ldots & 0 \\ C_{10} & 0 & C_{12} & \ldots & 0 \\ 0 & \ddots & \ddots & \ddots & \vdots \\ \vdots & & C_{N-1,N-2} & 0 & C_{N-1,N} \\ 0 & \ldots & & C_{N,N-1} & 0 \end{pmatrix},$$

where each element shown is a 4×4 matrix. The first row of each matrix corresponds to $n = 0$ and is derived from (6.3)–(6.4).

An eigenvalue problem is formed by rewriting the system as

$$-\mathcal{D}^{-1}\mathcal{C}\boldsymbol{v} = \frac{1}{\tau}\,\boldsymbol{v}, \tag{8.1}$$

where the eigenvalue $1/\tau$ must be real. Since the matrices have real entries, all eigenvalues are either real or occur in complex conjugate pairs.

For a given value of the wavenumber p, as well as parameters ν and κ from (3.1), the eigenvalue equation (8.1) yields a sequence of values for the forcing amplitude τ. In practice, we have found that choosing $N = 60$ terms in the series expansions is sufficient to ensure that the neglected coefficients are small (that is, the computed eigenvalues do not change appreciably when N is taken any larger than 60). The choices $\gamma = 0$ or $\gamma = \frac{1}{2}i$ are known as the harmonic and subharmonic cases, respectively, and any complex value of τ is discarded. These are the two cases that correspond to real Floquet multipliers, $e^{2\pi\gamma} = e^{2\pi(\alpha+i\beta)}$. When $0 < \beta < \frac{1}{2}$ on the other hand, the Floquet multipliers are complex and always correspond to solutions that are damped; hence, they are of no interest in our stability analysis.

The resulting harmonic and subharmonic eigenvalues correspond to physical modes of oscillation of the fiber which are *marginally stable*. We can then vary the wave number p, and produce a plot of each real value of τ, which traces out the boundary of the stability region of the linearized problem in parameter space. Furthermore, if we concentrate on the range $\tau \le \frac{1}{2}$, we need only consider stability boundaries that drop below the curve $\tau = \frac{1}{2}$.

Figures 8.1–8.3 depict the stability regions for various parameter values, with both harmonic (H) and subharmonic (S) modes shown. The stability boundaries separate

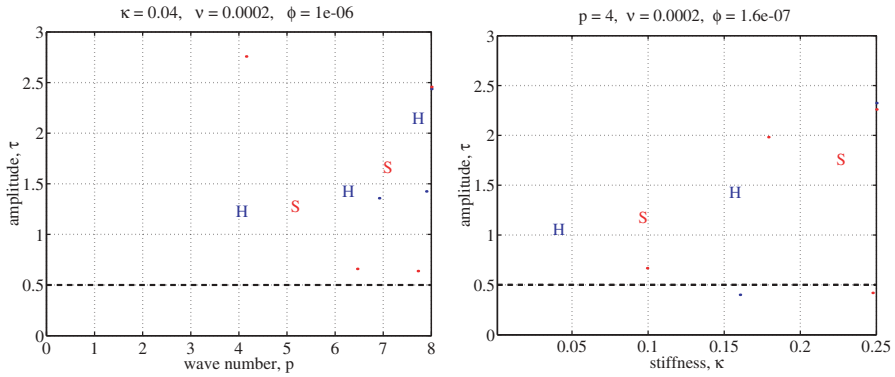

FIG. 8.1. *Stability diagrams, depicting plots of the fiber amplitude τ as a function of (left) wave number p, holding $\kappa = 0.04$; and (right) stiffness κ, holding $p = 4$. The other parameter values are $\nu = 0.0002$ and $\alpha = 0$. The curves traced out by the individual points represent the stability boundaries, and the regions above and inside each "tongue" correspond to unstable oscillations of the linearized IB problem. Regions of instability corresponding to harmonic modes (with $\gamma = 0$) are denoted "H" and are drawn with blue points, while the subharmonic modes (with $\gamma = \frac{1}{2}i$) are denoted "S" and are drawn with red points. The dashed horizontal line corresponds to $\tau = \frac{1}{2}$, and only portions of the tongues lying below this line correspond to oscillations with positive stiffness.*

parameter space into regions where the solution is stable and regions where it is unstable. Because of their distinctive shape, the regions of instability are usually referred to as "tongues." The unstable tongues alternate between harmonic and subharmonic modes, moving from left to right, with no overlap between the successive tongues.

Figure 8.1 shows two views of the stability regions for $\nu = 0.0002$: the first in the p, τ-plane with κ held constant at 0.04, and the second in the κ, τ-plane with $p = 4$. In both views, the tongue-like structure of the stability regions is apparent. The first unstable mode occurring for $\kappa = 0.04$ is a $p = 4$ mode, which corresponds to the left-most tongue that falls below the line $\tau = \frac{1}{2}$. Only tongues that correspond to integer values of the angular wavenumber p are physical. Notice in the right plot that increasing the stiffness has a stabilizing influence in the sense that the tongues migrate upward as κ is increased and therefore require higher-amplitude forcing in order to generate parametric resonance.

Figure 8.2 demonstrates more clearly the influence of changes in the stiffness parameter, by depicting the stability boundaries in the p, τ-plane for $\kappa = 0.02$, 0.04, and 0.08. As κ is increased (corresponding to a stiffer fiber), the regions of instability move towards the left, causing the wavenumber of the first unstable mode to decrease, periodically moving in and out of the "physical" regime.

The effect of changes in viscosity for constant stiffness is investigated in Figure 8.3, where plots for $\nu = 0.00005$, 0.0002, and 0.001 are given for $\kappa = 0.04$. As viscosity increases, the unstable regions migrate vertically upwards, so that the minimum value of τ corresponding to a linear instability increases, and some modes that were unstable no longer lead to parametric resonance. As a result, larger-amplitude forcing is necessary to cause onset of parametric resonance in fibers with larger viscosity. If ν is taken large enough that all tongues lift above the $\tau = \frac{1}{2}$ line, then the system is no longer subject to parametric resonance. These results are evidence of the fact that viscosity has a stabilizing influence on the system.

In the limit as $\nu \to 0$, the tongues extend down to the p-axis, where they touch the

line $\tau = 0$, corresponding to unforced oscillations of the immersed fiber. Therefore, the points where the tongues touch down in the $\nu = 0$ limit represent the natural modes of oscillation which were discussed in detail in section 7.

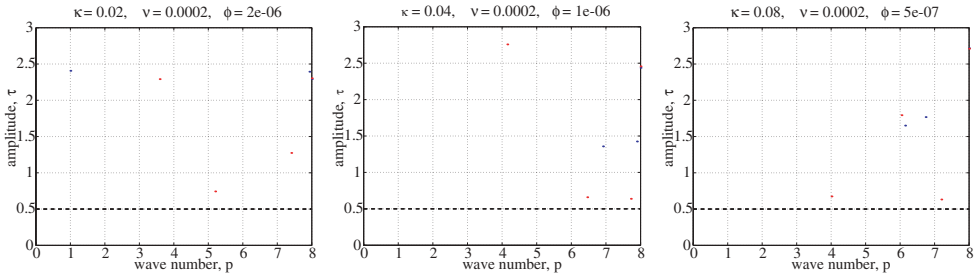

FIG. 8.2. *A series of three plots showing the impact of changes in the stiffness on the stability boundaries in the* p, τ*-plane, with viscosity* $\nu = 0.0002$ *and three different values of stiffness:* $\kappa = 0.02$ *(left),* 0.04 *(middle), and* 0.08 *(right).*

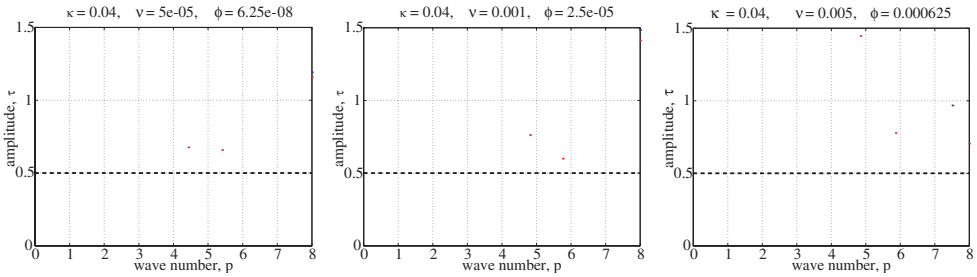

FIG. 8.3. *A series of three plots showing the impact of changes in viscosity in the stability boundaries in the* p, τ*-plane, with stiffness* $\kappa = 0.04$ *and three different values of viscosity:* $\nu =$ 0.00005 *(left),* 0.001 *(middle), and* 0.005 *(right).*

9. Comparison with IB computations. In this section, we use several immersed boundary computations to demonstrate the validity of the preceding Floquet analysis. The numerical method is based on a straightforward discretization of the IB equations in terms of velocity and pressure variables. An alternating direction implicit (ADI) approach is used to apply the convection, diffusion, and forcing terms to obtain an intermediate velocity field. The resulting velocity is then made divergence-free through the use of a split-step pressure projection procedure. The standard cosine approximation to the Dirac delta function is employed [20], which is smoothed over a square box with side length of four fluid grid points. The resulting method is second-order accurate in space, except for the approximate delta function interpolation which limits the spatial accuracy to first order. The method is explicit and has first-order accuracy in time. There are many variants of the IB method that increase both spatial and temporal accuracy, but we have chosen instead to demonstrate the presence of parametric resonance using this simplest and most common implementation. For complete details of the numerical technique, refer to [20] or [24].

All computations were performed on an immersed boundary whose rest configuration is a circle, immersed in a periodic box of dimension 2.5 times the size of the circular boundary. The analysis strictly applies only to an infinite fluid domain, but we found that this domain size was large enough in practice to avoid significant

TABLE 9.1
Parameters for the two resonant cases, one with a first unstable mode with angular wavenumber $p = 2$, and the other with $p = 4$.

Case I	Case II
$\kappa = 0.5$	$\kappa = 0.04$
$\nu = 0.004$	$\nu = 0.00056$
$\phi = 3.2 \times 10^{-5}$	$\phi = 7.84 \times 10^{-6}$
$\rho = 1$	$\rho = 1$
$\mu = 0.4$	$\mu = 0.5$
$R = 0.2$	$R = 1$
$K_c = 125000$	$K_c = 40000$
$\omega_o = 2500$	$\omega_o = 900$
$\tau = 0.45$	$\tau = 0.45$
$p = 2$ unstable	$p = 4$ unstable

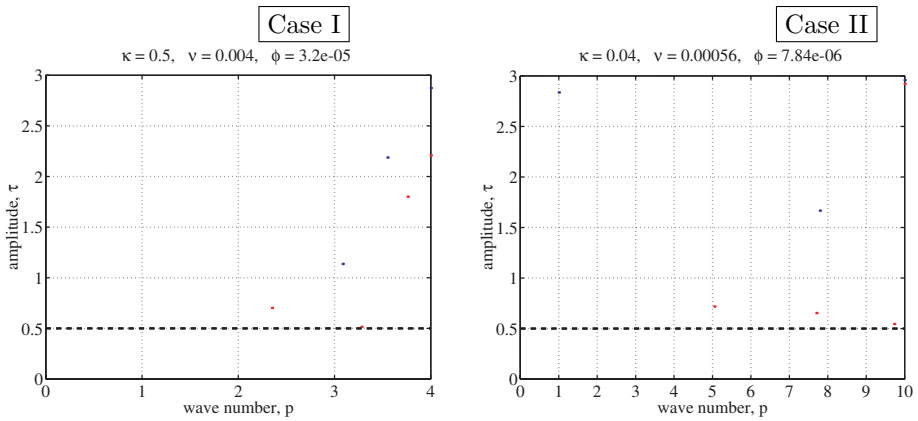

FIG. 9.1. *Stability diagrams for Case* I *($\kappa = 0.5$, $\nu = 0.004$) and Case* II *($\kappa = 0.04$, $\nu = 0.00056$).*

interference from neighboring periodic copies. The fluid domain is divided into a 64×64 grid with 192 immersed boundary points, ensuring that there is significant resolution of the boundary within each fluid grid cell. Finer grid computations were also performed with a 128×128 fluid grid and 384 fiber points to validate the results. The time step was selected to be well within the stability restriction imposed by the explicit method.

We chose to focus on two specific sets of parameters for which the stability plots suggested different resonant p-modes. The parameters are listed in Table 9.1, and the corresponding stability regions are displayed in Figure 9.1. In Case I, the first unstable tongue corresponds to a harmonic mode of oscillation at $p = 2$, while the lowest-wavenumber unstable mode for the second case is $p = 4$ (also harmonic).

We next present numerical evidence that supports the existence of these two instances of parametric resonance. In both cases, the immersed boundary is initially in the shape of a circle of radius R with a radial perturbation of the form $r = R(1 + 0.05\cos(p\theta))$. The results of a given simulation are reported as plots of $\hat{r}_p(t)$, which represents the amplitude of the p-mode of oscillation in the fiber versus time, and is calculated as follows:

1. we convert the (x, y) position of each point on the immersed fiber to radial coordinates;

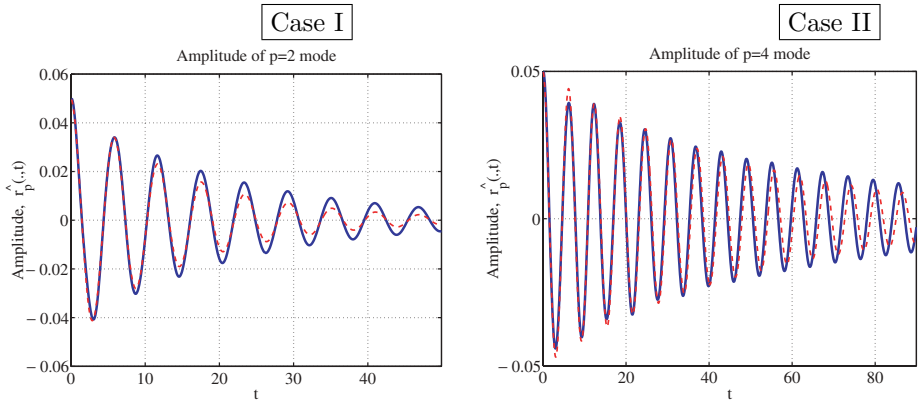

FIG. 9.2. *Amplitude of the unforced immersed boundary for Case* I *($p = 2$) and Case* II *($p = 4$). The dashed curve is an approximate fit to the computed results using a function of the form $e^{\alpha t}\cos(\beta t)$.*

2. using cubic splines, we interpolate the points representing the fiber positions onto a set of points that are equally spaced in θ;
3. we calculate $\hat{r}_p(t) = FFT_\theta(r(\theta, t))$, the fast Fourier transform of the radius in θ, which then yields the amplitude of the desired p-mode.

First, we present plots of the unforced solution (with $\tau = 0$) in Figure 9.2 that represent the natural mode of oscillation for the fiber in each case. The rate of decay and frequency of the natural modes of oscillation for the unforced fiber are as follows:

$$\text{Case I:} \quad \alpha = -0.066, \qquad \beta = 1.071,$$
$$\text{Case II:} \quad \alpha = -0.020, \qquad \beta = 1.016.$$

When the immersed boundary is then forced internally at a frequency equal to the resonant frequency suggested by the plots in Figure 9.1 (i.e., $\omega_o = 2500$ in Case I and $\omega_o = 900$ in Case II), amplitude of oscillation grows far beyond the initial amplitude of 0.05 cm. The motion never actually becomes unstable, but the fiber instead exhibits sustained, large-amplitude oscillations (see Figure 9.3 and compare to Figure 9.2).

In order to verify that this behavior is truly arising from a parametric resonance, we consider changes to either κ or ν that move the resonant tongue in the eigenvalue plot outside the range of parameters being considered. The results are summarized in Figures 9.4 and 9.5. the As the viscosity is increased, the oscillations either decrease in amplitude or decay in time, though not at as rapid a rate as for the unforced case. Because an increase in viscosity acts to raise the "tongues" in the eigenvalue plot, this is precisely the behavior we would expect.

Alternately, if we increase or decrease the value of κ in relation to the resonant value, the resulting oscillations are pictured in Figure 9.5. The amplitude of oscillation for the resonant mode has a maximum value close to the resonant value of κ, which represents the movement of the resonant tongues either to the left or to the right as κ is increased or decreased, respectively.

The effect of varying the stiffness perturbation amplitude τ is displayed in Figure 9.6 for Case II. For $\tau \leq 0.40$, there is no longer a sustained oscillation in the fiber, and as τ is reduced the amplitude of the fiber motion decreases.

At this point, it is important to emphasize that in our numerical simulations, resonance is indicated by sustained, large-amplitude motions, rather than any actual

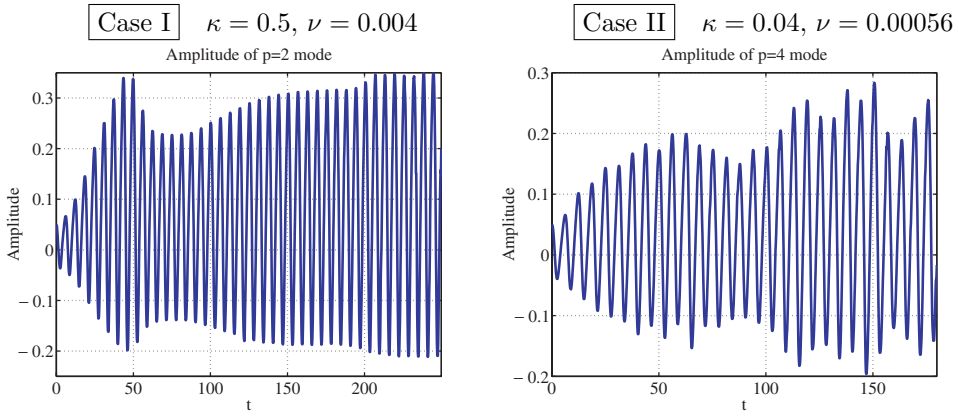

FIG. 9.3. *Amplitude of the resonant p-mode, when the immersed boundary is forced at the resonant frequency ($p = 2$ for Case* I *and $p = 4$ for Case* II*). Both cases display a sustained, large-amplitude oscillation.*

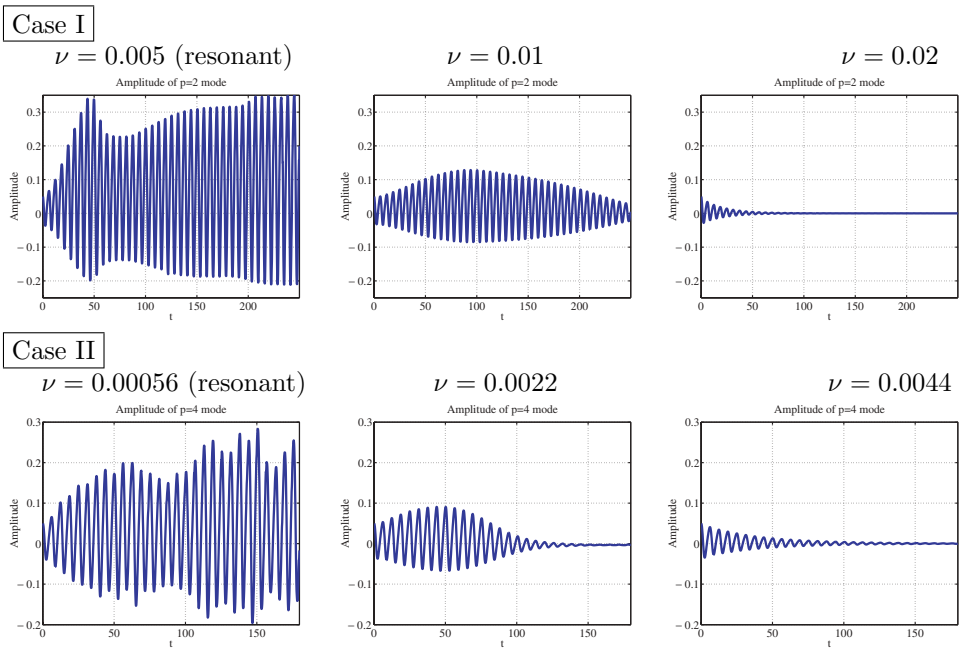

FIG. 9.4. *Amplitude of the resonant p-mode in Cases* I *and* II*, as ν is increased. The stabilizing influence of viscosity is exhibited by the inability of the fiber to sustain large-amplitude oscillations for even small increases in the viscosity.*

instability (i.e., unbounded oscillations). This discrepancy arises from both numerical errors and simplifications to the model, namely:

- the numerical scheme is only first order in space and time and introduces a significant level of artificial viscosity;
- although the fiber force term in the linearized Navier–Stokes equations was also linearized in the forgoing analysis, it is actually nonlinear, which acts to

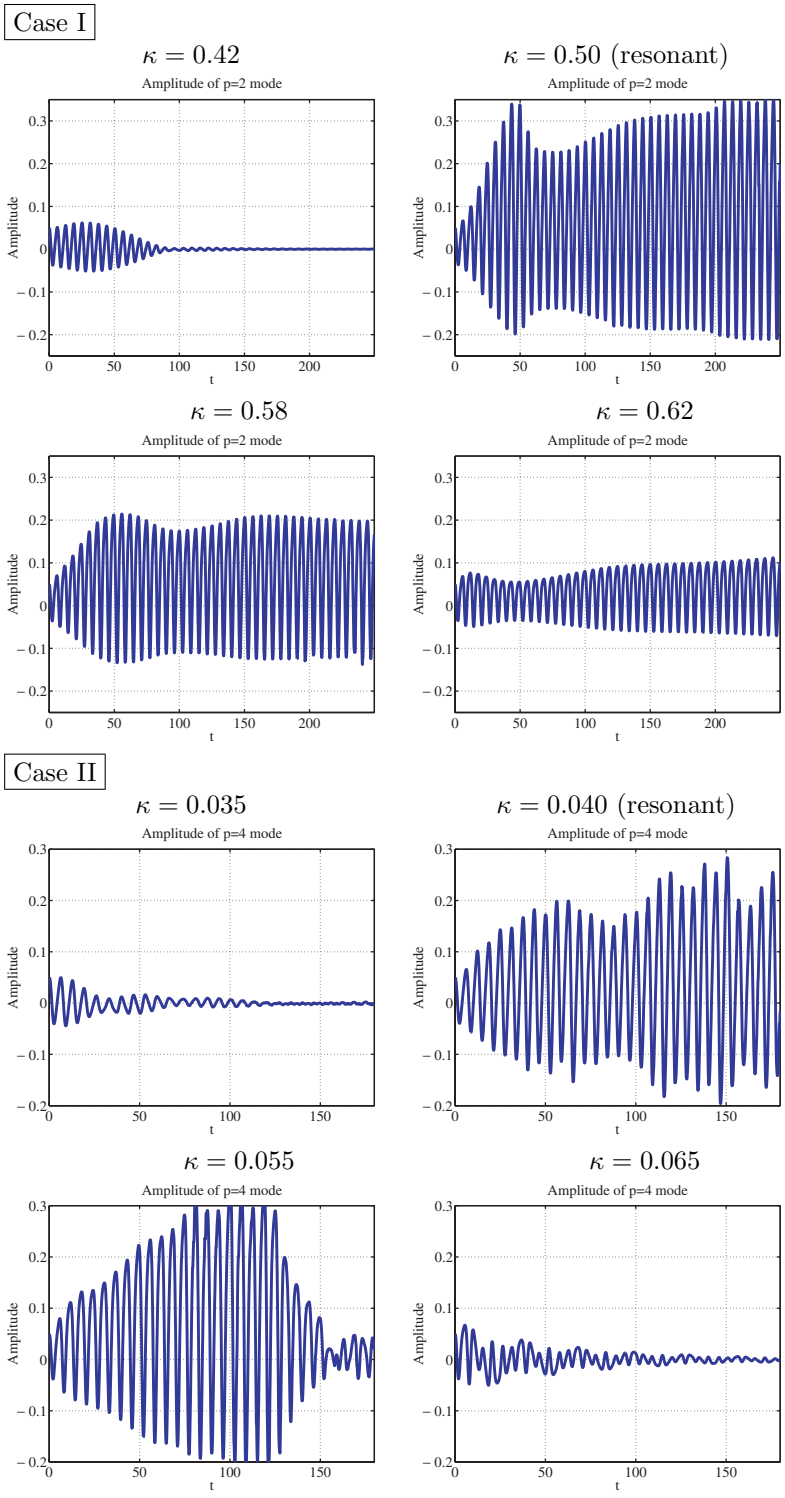

FIG. 9.5. *Amplitude of the resonant p-mode in Cases* I *and* II, *as* κ *is varied. When the stiffness is taken either smaller or larger than the resonant value, the amplitude of the oscillations decreases to the point that they can no longer be sustained.*

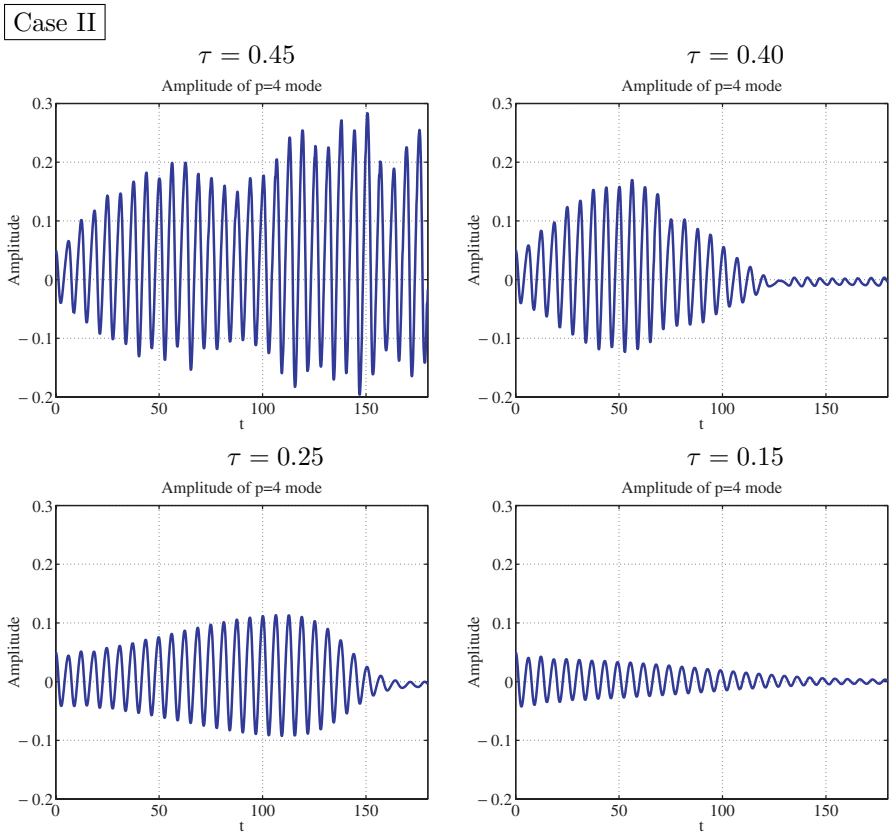

FIG. 9.6. *Amplitude of the resonant p-mode in Case* II*, as the forcing amplitude,* τ*, is varied. As the forcing is reduced, the amplitude of the fiber oscillations also diminishes.*

stabilize the numerical results;

- the analysis assumed an infinite fluid domain, while our numerical simulations use periodic boundary conditions. Discrepancies owing to interference from periodic copies of the immersed fiber are therefore unavoidable, though we have attempted to choose the size of our computational domain large enough so that these errors are minimized.

A further symptom of these errors is the fact that the stability boundaries in parameter space demonstrated in the simulations are not nearly as sharp, or located in exactly the same locations, as indicated by the plots in section 8. Nonetheless, the correspondence between analytical and numerical results is still quite convincing evidence of the presence of parametric resonance in the linearized IB problem.

The final set of results indicates what transpires when a mode other than the resonant mode is excited initially. We restrict ourselves to Case II and initialize the fiber position with modes having wavenumber $p = 2$ or $p = 3$, while still forcing the stiffness through a $p = 4$ mode. The other parameters remain the same as in the resonant case. Figure 9.7 shows that in both cases, the given 2- and 3-modes do not grow; however, energy transfers over time into the resonant $p = 4$ mode which eventually dominates the fiber oscillation.

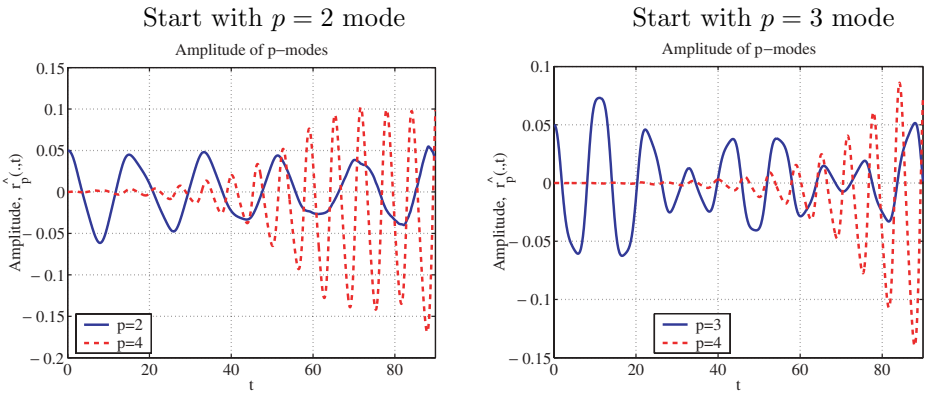

FIG. 9.7. *The amplitude of various fiber modes in Case* II *when wavenumbers* $p = 2$ *and* $p = 3$ *are excited initially instead of the* $p = 4$ *mode. Numerical errors give rise to phase-shifted oscillations which, when combined linearly with the initial conditions, perturb the* $p = 4$ *mode and hence feed energy into the resonant mode over time.*

10. Conclusions. Floquet analysis has proven to be an extremely useful tool in examining parametric resonance and the stability behavior of a wide variety of flows involving interfaces and fluid-structure interaction. In this paper, we study parametric resonances arising from an elastic membrane immersed in a viscous fluid in two dimensions, which is driven by periodic variations in the stiffness parameter of the elastic material. The underlying mathematical model, known as the immersed boundary formulation, captures not only the flow-induced deformations of the elastic membrane but also the influence of the immersed structure on the surrounding fluid flow. To our knowledge, this is the first study of its kind that captures this two-way interaction between fluid and fiber in a parametrically forced system.

Our Floquet analysis leads to an eigenvalue problem that can be solved in order to determine the stability boundaries in parameter space that separate the regions in which the motion is stable from those in which it is unstable. Using asymptotic expansions of the resulting solutions, we demonstrate that our results are consistent with previous analyses of unforced immersed fibers. The decay rates and frequencies of oscillation for the forced system are also shown to match closely those found in full numerical simulations of the fluid-fiber system for small-wavenumber perturbations. We also present numerical results that verify the existence of resonances in parametrically forced immersed boundaries.

This study opens the door for several avenues of further investigation. First of all, while we have demonstrated the existence of parametric resonances numerically in periodically forced immersed fibers, we have yet to find a biological system in which the parameters lie within the unstable regime. In the heart, for example, the muscle fiber stiffness appears to be too small to lead to parametric resonance, according to our analysis. However, we intend to investigate other biological systems with different parameter ranges to determine if resonances are possible.

There are also several natural extensions to the analysis that would allow us to investigate much more interesting fiber dynamics. For example, introducing a spatial dependence in the stiffness, $K(s,t)$, would better mimic biological systems in which an active fiber is pulsed via a wave of contraction that travels around the fiber. However, this form of the stiffness complicates the Floquet analysis significantly by coupling the various fiber modes, and hence would require an extension of our analytical technique.

We also intend to investigate the use of optimal control to see whether it is possible to eliminate parametric resonances by introducing an additional periodic forcing term in the system.

Appendix A. Some useful Bessel function formulas. The following identities are taken from [27] and [1]:

$$J_p(z) = \frac{z}{2p}(J_{p-1}(z) + J_{p+1}(z)), \tag{A.1}$$

$$J_p'(z) = \frac{1}{2}(J_{p-1}(z) - J_{p+1}(z)), \tag{A.2}$$

$$\int z^{p+1} J_p(az)dz = \frac{z^{p+1}}{a} J_{p+1}(az), \tag{A.3}$$

$$\int z^{1-p} J_p(az)dz = \frac{-z^{1-p}}{a} J_{p-1}(az). \tag{A.4}$$

Equations (A.1)–(A.4) are written for the Bessel function of the first kind, $J_p(z)$, but are also valid for the various other Bessel functions, $Y_p(z)$, $H_p(z)$, etc.

Appendix B. Proof of Claim 1.

CLAIM 1. *Given the expansions in* (3.3a) *and* (3.3b)*,*

$$(\hat{\boldsymbol{z}} \cdot \nabla \times \boldsymbol{f}^{(0)}) = 0 \qquad \textit{and}$$
$$(\hat{\boldsymbol{z}} \cdot \nabla \times \boldsymbol{f}^{(1)}) = K\left(X^{\theta}_{ss} + X^{r}_{s}\right)\left(\frac{\delta(r-1)}{r}\right)_r - K\left(X^{r}_{sss} - X^{\theta}_{ss}\right)\frac{\delta(r-1)}{r}.$$

Proof. Since

$$\begin{aligned}(\hat{\boldsymbol{z}} \cdot \nabla \times \boldsymbol{f}) &= -\hat{\boldsymbol{z}} \cdot \int_0^{2\pi} (K\boldsymbol{X}_s)_s \times \nabla\delta(\boldsymbol{x} - \boldsymbol{X})\, ds \\ &= -\int_0^{2\pi} [\hat{\boldsymbol{z}} \times (K\boldsymbol{X}_s)_s] \cdot \nabla\delta(\boldsymbol{x} - \boldsymbol{X})\, ds,\end{aligned}$$

we have that (3.3a)–(3.3b) imply that

$$\begin{aligned}(\hat{\boldsymbol{z}} \cdot \nabla \times \boldsymbol{f}^{(0)}) &= -\int_0^{2\pi} [\hat{\boldsymbol{z}} \times (K(t)\hat{\boldsymbol{r}}_s)_s] \cdot \nabla\delta(\boldsymbol{x} - \boldsymbol{X}(s,t))\, ds \\ &= -K(t)\int_0^{2\pi} [\hat{\boldsymbol{z}} \times \hat{\boldsymbol{r}}_{ss}] \cdot \nabla\delta(\boldsymbol{x} - \boldsymbol{X}(s,t))\, ds \\ &= -K(t)\int_0^{2\pi} \frac{d}{ds}\delta(\boldsymbol{x} - \boldsymbol{X}(s,t))\, ds \; = 0.\end{aligned}$$

We also have that

$$\begin{aligned}(\hat{\boldsymbol{z}} \cdot \nabla \times \boldsymbol{f}^{(1)}) &= -\int_0^{2\pi} \left[\hat{\boldsymbol{z}} \times (K\boldsymbol{X}^{(1)}_s)_s\right] \cdot \nabla\delta(\boldsymbol{x} - \boldsymbol{X}^{(0)})\, ds \\ &\quad + \int_0^{2\pi} \left\{\left[\hat{\boldsymbol{z}} \times (K\boldsymbol{X}^{(0)}_s)_s\right] \cdot \nabla\right\}\left(\boldsymbol{X}^{(1)} \cdot \nabla\right)\delta(\boldsymbol{x} - \boldsymbol{X}^{(0)})\, ds \\ &= I_1 + I_2.\end{aligned} \tag{B.1}$$

The second term can be simplified:

$$\begin{aligned} I_2 &= K\int_0^{2\pi}\left(\boldsymbol{X}^{(1)}\cdot\nabla\right)\left\{\left[\hat{\boldsymbol{z}}\times\boldsymbol{X}_{ss}^{(0)}\right]\cdot\nabla\right\}\delta(\boldsymbol{x}-\boldsymbol{X}^{(0)})\,ds \\ &= K\int_0^{2\pi}\left(\boldsymbol{X}^{(1)}\cdot\nabla\right)\frac{d}{ds}\delta(\boldsymbol{x}-\boldsymbol{X}^{(0)})\,ds \\ &= -K\int_0^{2\pi}\boldsymbol{X}_s^{(1)}\cdot\nabla\delta(\boldsymbol{x}-\boldsymbol{X}^{(0)})\,ds, \end{aligned}$$

so that so far we have that (B.1) is

$$(\hat{\boldsymbol{z}}\cdot\nabla\times\boldsymbol{f}^{(1)}) = -K\int_0^{2\pi}\left[\hat{\boldsymbol{z}}\times\boldsymbol{X}_{ss}^{(1)}+\boldsymbol{X}_s^{(1)}\right]\cdot\nabla\delta(\boldsymbol{x}-\boldsymbol{X}^{(0)})\,ds.$$

Now it is convenient to write $\boldsymbol{X}^{(1)}$ in polar coordinates

$$\boldsymbol{X}^{(1)} = X^r(s,t)\hat{\boldsymbol{r}}(s)+X^\theta(s,t)\hat{\boldsymbol{\theta}}(s),$$

so that

$$\hat{\boldsymbol{z}}\times\boldsymbol{X}_{ss}^{(1)}+\boldsymbol{X}_s^{(1)} = -\left(X_{ss}^\theta+X_s^r\right)\hat{\boldsymbol{r}}+\left(X_{ss}^r-X_s^\theta\right)\hat{\boldsymbol{\theta}}.$$

Now we can write

$$\begin{aligned} (\hat{\boldsymbol{z}}\cdot\nabla\times\boldsymbol{f}^{(1)}) &= K\int_0^{2\pi}\left[X_{ss}^\theta+X_s^r\right]\hat{\boldsymbol{r}}\cdot\nabla\delta(\boldsymbol{x}-\boldsymbol{X}^{(0)})\,ds \\ &\quad - K\int_0^{2\pi}\left[X_{ss}^r-X_s^\theta\right]\hat{\boldsymbol{\theta}}\cdot\nabla\delta(\boldsymbol{x}-\boldsymbol{X}^{(0)})\,ds. \end{aligned}$$

The last term can be integrated by parts and we arrive at

$$\begin{aligned} (\hat{\boldsymbol{z}}\cdot\nabla\times\boldsymbol{f}^{(1)}) &= \int_0^{2\pi}K\left(X_{ss}^\theta+X_s^r\right)\,\hat{\boldsymbol{r}}\cdot\nabla\delta(\boldsymbol{x}-\boldsymbol{X}^{(0)})\,ds \\ &\quad - \int_0^{2\pi}K\left(X_{sss}^r-X_{ss}^\theta\right)\,\delta(\boldsymbol{x}-\boldsymbol{X}^{(0)})\,ds. \end{aligned}$$

If we now write

$$\delta(\boldsymbol{x}-\boldsymbol{X}^{(0)}) = \frac{\delta(r-1)\delta(\theta-s)}{r},$$

we get

$$\begin{aligned} (\hat{\boldsymbol{z}}\cdot\nabla\times\boldsymbol{f}^{(1)}) &= \left[K\left(X_{ss}^\theta+X_s^r\right)\right](\theta,t)\,\left(\frac{\delta(r-1)}{r}\right)_r \\ &\quad - \left[K\left(X_{sss}^r-X_{ss}^\theta\right)\right](\theta,t)\,\frac{\delta(r-1)}{r}. \qquad \square \end{aligned}$$

Appendix C. Jump conditions. The derivation of the jump conditions for vorticity will make use of the following result.

CLAIM 2. *In the sense of distributions*

$$r\left(\frac{\delta(r-R)}{r}\right)' = \delta'(r-R) - \frac{\delta(r-R)}{R}.$$

Proof. Let $\phi(r)$ be a smooth function. Then

$$\begin{aligned}\int \phi(r)\, r\left(\frac{\delta(r-R)}{r}\right)' dr &= -\int \left(r\phi(r)\right)_r \left(\frac{\delta(r-R)}{r}\right) dr \\ &= -\int \left(\phi'(r) + \frac{\phi(r)}{r}\right)\delta(r-R)\, dr \\ &= -\phi'(R) - \frac{\phi(R)}{R}.\end{aligned}$$

The result follows. ∎

The jump conditions for an equation of the form

$$-\frac{1}{r}(r\xi')' + \left(\frac{(\gamma+in)}{\nu} + \frac{p^2}{r^2}\right)\xi = A\left(\frac{\delta(r-1)}{r}\right)' + B\left(\frac{\delta(r-1)}{r}\right),$$

where A and B are independent of r, can be derived as follows. We first multiply the equation by r:

$$-(r\xi')' + \left(\frac{(\gamma+in)}{\nu}r + \frac{p^2}{r}\right)\xi = Ar\left(\frac{\delta(r-1)}{r}\right)' + B\delta(r-1),$$

and use the claim to write it as

$$-(r\xi')' + \left(\frac{(\gamma+in)}{\nu}r + \frac{p^2}{r}\right)\xi = A\delta'(r-1) + (B-A)\delta(r-1).$$

We now integrate from $1-\epsilon$ to some point r to get

$$-\left[r\xi'(r) - (1-\epsilon)\xi'(1-\epsilon)\right] + \int_{1-\epsilon}^{r}\left(\frac{(\gamma+in)}{\nu}q + \frac{p^2}{q}\right)\xi(q)\, dq = A\delta(r-1) + (B-A)H(r-1). \tag{C.1}$$

We can use (C.1) in two ways. First, set $r = 1+\epsilon$ and take the limit $\epsilon \to 0$:

$$-[\![\xi']\!] = (B-A). \tag{C.2}$$

Second, we divide (C.1) by r, integrate from $1-\epsilon$ to $1+\epsilon$, and let $\epsilon \to 0$ to get

$$-[\![\xi]\!] = A. \tag{C.3}$$

Equations (C.2)–(C.3) are the two jump conditions.

Appendix D. Solution of the stream function equation. In this section we describe the method for finding the solution of the stream function equation

$$-\frac{1}{r}\left(r\psi_r\right)_r + \frac{p^2}{r^2}\psi = \xi(r),$$

where $\xi(r)$ is given by

$$\xi(r) = \begin{cases} bJ_p(i\Omega_n r) & \text{if } r < 1 \qquad \text{(inner)}, \\ aH_p(i\Omega_n r) & \text{if } r > 1 \qquad \text{(outer)}. \end{cases}$$

The general solution may be written as

$$\psi(r) = \int_0^\infty \xi(r)\mathcal{G}(r,z)dz.$$

Here, the Green's function $\mathcal{G}(r,z)$ is the solution of

$$-\frac{1}{r}\left(r\mathcal{G}_r\right)_r + \frac{p^2}{r^2}\mathcal{G} = \delta(r-z). \tag{D.1}$$

Multiplying this equation by r, integrating from $z-\epsilon$ to $z+\epsilon$, and taking the limit $\epsilon \to 0$, we find that $\mathcal{G}(r,z)$ satisfies the jump conditions

$$[\![\mathcal{G}]\!] = 0 \qquad \text{and} \qquad [\![\mathcal{G}_r]\!] = -1.$$

Since solutions of equation (D.1) are of the form r^p and r^{-p}, we have that

$$\mathcal{G}(r,z) = \frac{z}{2p}\begin{cases} \dfrac{r^p}{z^p} & \text{if } r < z, \\ \dfrac{z^p}{r^p} & \text{if } r > z. \end{cases}$$

The stream function is then found by piecewise integration. For the interior solution, $r < 1$, we obtain

$$\begin{aligned} \psi(r) &= \frac{b}{2pr^p}\int_0^r J_p(i\Omega_n r')(z)^{p+1}\,dz + \frac{br^p}{2p}\int_r^1 J_p(i\Omega_n r')(z)^{1-p}\,dz \\ &\quad + \frac{ar^p}{2p}\int_1^\infty H_p(i\Omega_n r')(z)^{1-p}\,dz \\ &= \frac{br}{2ip\Omega_n}\Big[J_{p-1}(i\Omega_n r) + J_{p+1}(i\Omega_n r)\Big] + \frac{r^p}{2ip\Omega_n}\Big[aH_{p-1}(i\Omega_n) - bJ_{p-1}(i\Omega_n)\Big], \end{aligned}$$

making use of the identities (A.3) and (A.4). The solution for $r > 1$ is found in the same way.

REFERENCES

[1] M. Abramowitz and I. A. Stegun, *Handbook of Mathematical Functions with Formulas, Graphs and Mathematical Tables*, John Wiley and Sons, New York, 1972.

[2] K. M. Arthurs, L. C. Moore, C. S. Peskin, E. B. Pitman, and H. E. Layton, *Modeling arteriolar flow and mass transport using the immersed boundary method*, J. Comput. Phys., 147 (1998), pp. 402–440.

[3] R. P. Beyer and R. J. LeVeque, *Analysis of a one-dimensional model for the immersed boundary method*, SIAM J. Numer. Anal., 29 (1992), pp. 332–364.

[4] R. Cortez and M. Minion, *The blob projection method for immersed boundary problems*, J. Comput. Phys., 161 (2000), pp. 428–453.

[5] R. Cortez and D. A. Varela, *The dynamics of an elastic membrane using the impulse method*, J. Comput. Phys., 138 (1997), pp. 224–247.

[6] S. M. Curry, *How children swing*, Amer. J. Phys., 44 (1976), pp. 924–926.

[7] R. Dillon and L. Fauci, *Microscale model of bacterial and biofilm dynamics in porous media*, Biotechnol. and Bioengrg., 68 (2000), pp. 536–547.
[8] L. J. Fauci, *A computational model of the fluid dynamics of undulator and flagellar swimming*, Amer. Zool., 36 (1996), pp. 599–607.
[9] P. Martin, A. D. Mehta, and A. J. Hudspeth, *Negative hair-bundle stiffness betrays a mechanism for mechanical amplification by the hair cell*, Proc. Nat. Acad. Sci. USA, 97 (2000), pp. 12026–12031.
[10] Y. Kim and C. S. Peskin, 2-*D parachute simulation by the immersed boundary method*, manuscript, Courant Institute of Mathematical Sciences, New York University, New York, 2001.
[11] K. Kumar and L. S. Tuckerman, *Parametric instability of the interface between two fluids*, J. Fluid Mech., 279 (1994), pp. 49–68.
[12] M.-C. Lai, *Simulations of the Flow Past an Array of Circular Cylinders as a Test of the Immersed Boundary Method*, Ph.D. thesis, New York University, New York, 1998.
[13] M.-C. Lai and Z. Li, *A remark on jump conditions for the three-dimensional Navier-Stokes equations involving an immersed moving membrane*, Appl. Math. Lett., 14 (2001), pp. 149–154.
[14] O. Lioubashevski, J. Fineberg, and L. S. Tuckerman, *Scaling of the transition to parametrically driven surface waves in highly dissipative systems*, Phys. Rev. E (3), 55 (1997), pp. 3832–3835.
[15] G. McKay, *Onset of double-diffusive convection in a saturated porous layer with time-periodic surface heating*, Contin. Mech. Thermodyn., 10 (1998), pp. 241–251.
[16] L. A. Miller, *A mathematical model of insect flight: The immersed boundary method with fling*, Amer. Zool., 40 (2000), p. 1133.
[17] H. W. Müller, H. Wittmer, C. Wagner, J. Albers, and K. Knorr, *Analytic stability theory for Faraday waves and the observation of the harmonic surface response*, Phys. Rev. Lett., 78 (1997), pp. 2357–2360.
[18] A. H. Nayfeh and D. T. Mook, *Nonlinear Oscillations*, John Wiley and Sons, New York, 1979.
[19] C. S. Peskin, *Linearized Immersed Boundary*, unpublished notes.
[20] C. S. Peskin, *The immersed boundary method*, in Acta Numerica, Acta Numer. 11, Cambridge University Press, Cambridge, UK, 2002, pp. 1–39.
[21] C. S. Peskin and D. M. McQueen, *A three-dimensional computational model for blood flow in the heart.* I. *Immersed elastic fibers in a viscous incompressible fluid*, J. Comput. Phys., 81 (1989), pp. 372–405.
[22] C. S. Peskin and B. F. Printz, *Improved volume conservation in the computation of flows with immersed boundaries*, J. Comput. Phys., 105 (1993), pp. 33–46.
[23] C. Semler and M. P. Païdoussis, *Nonlinear analysis of the parametric resonances of a planar fluid-conveying cantilevered pipe*, J. Fluids Struct., 10 (1996), pp. 787–825.
[24] J. M. Stockie, *Analysis and Computation of Immersed Boundaries, with Application to Pulp Fibres*, Ph.D. thesis, Institute of Applied Mathematics, University of British Columbia, Vancouver, BC, Canada, 1997; also available online from http://www.iam.ubc.ca/theses/stockie/stockie.html.
[25] J. M. Stockie and S. I. Green, *Simulating the motion of pulp fibers using the immersed boundary method*, J. Comput. Phys., 147 (1998), pp. 147–165.
[26] J. M. Stockie and B. T. R. Wetton, *Stability analysis for the immersed fiber problem*, SIAM J. Appl. Math., 55 (1995), pp. 1577–1591.
[27] C. J. Tranter, *Bessel Functions with Some Physical Applications*, Hart Publishing, New York, 1968.
[28] X. Wang, *Instability analysis of some fluid-structure interaction problems*, Comput. & Fluids, 32 (2003), pp. 121–138.
[29] L. Zhu and C. S. Peskin, *Simulation of a flapping flexible filament in a flowing soap film by the immersed boundary method*, J. Comput. Phys., 179 (2002), pp. 452–468.